X-ray radiation-induced damage in DNA monitored by online Raman

John E. McGeehan,[a]* **Philippe Carpentier,**[b,c] **Antoine Royant,**[b,c]
Dominique Bourgeois[b,c] **and Raimond B. G. Ravelli**[a]*

[a]EMBL, 6 rue Jules Horowitz, BP 181, 38042 Grenoble CEDEX 9, France, [b]Institut de Biologie
Structurale, CNRS/CEA/UJF, UMR 5075, 41 rue Jules Horowitz, 38027 Grenoble CEDEX 1, France,
and [c]ESRF, 6 Rue Jules Horowitz, BP 220, 38043 Grenoble CEDEX, France.
E-mail: mcgeehan@embl.fr, ravelli@embl.fr

High-quality Raman spectra have been collected on single DNA crystals kept at
100 K in a flow of cold nitrogen gas prior, during and after macromolecular
crystallography (MX) data collection. The non-symmetric bending vibration for
C—Br bonds in 8-bromo-2′-deoxyguanosine has been unambiguously identified
at 293 cm^{-1} in the non-resonant Raman spectra. The breakage of this bond
could be monitored by the continuous recording of Raman spectra during X-ray
exposure, and its decay *versus* dose could be directly correlated with the loss of
the bromide definition within the electron-density maps as determined with MX.

1. Introduction

The interaction of ionizing radiation such as X-rays, electrons
and γ-rays with biological tissue causes damage initiated by
free radicals. Much effort has been invested in trying to
understand the mechanisms involved, in particular for DNA.
High-energy radiation induces its molecular damage as a
result of a multitude of low-energy events (Michael & O'Neill,
2000; Boudaiffa *et al.*, 2000). This has triggered wide interest in
understanding the effects of low-dose radiation to cells and
molecules.

The advent of powerful X-ray sources at third-generation
synchrotron undulator beamlines has generated interest in
radiation damage from another group of scientists for a
completely different reason. Although these modern beam-
lines have made an extraordinary impact in structural biology,
they also reveal the painful problem of radiation damage,
which quickly reduces the diffractive power of cryocooled
crystals. Macromolecular crystallography (MX) is rapidly
reaching the state, as in electron microscopy (EM), where the
resolution of the final model becomes solely determined by
radiation damage. This has brought the subject to the fore-
front of the attention of structural biologists.

The doses used in MX and EM on cryocooled samples
(MGy) are incomparable with those used while studying the
effects on living tissue (mGy–kGy). Nevertheless, some
parallels exist. Structural observation of the 'fingerprint' that
X-rays leave on macromolecules (Ravelli & McSweeney, 2000;
Burmeister, 2000; Weik *et al.*, 2000) shows some striking
similarities with findings from traditional (low-dose) pulsed
radiolysis studies, *e.g.* the breakage of disulfide bonds has been
reported in low-dose pulse radiolysis studies on protein solu-
tions (Ramakrishna *et al.*, 1983; Favaudon *et al.*, 1990; Symons,
1995), for crystals from which MX data were collected at room
temperature at an in-house source (Helliwell, 1988), as well as
for cryocooled crystals from which data were collected at
synchrotrons (Ravelli & McSweeney, 2000; Burmeister, 2000;
Weik *et al.*, 2000).

Radiation chemists and biologists have predominantly
studied DNA because it is the central macromolecule for
genetic information exchange and its stability and resistance
to free radicals have direct consequences for human health.
After the primary absorption event, tracks of energetically
charged particles set in motion low-energy electrons that
transfer their energy to the DNA molecule. Several studies
have attempted to understand how low-energy electrons
damage DNA molecules, mainly by analysing single- and
double-strand breaks (SSB, DSB) upon irradiation (Boudaiffa
et al., 2000; Michael & O'Neill, 2000). Fragmentation of the
various DNA components (base, deoxyribose and phosphate)
is initiated by resonant electron attachment, and followed by
reactions occurring over distances comparable with the
double-strand diameter of the DNA. The understanding of the
early events in the generation of genotoxic damage is still far
from complete. A better understanding of these early events
may eventually allow one to manipulate the effects of ionizing
radiation at a molecular level.

It could be of great interest if MX were able to obtain new
insight into the detailed structural consequences of early
events of radiation damage to DNA. DNA and RNA struc-
tures are well studied with over 3000 entries within the nucleic
acid database; approximately two-thirds were solved by MX,

often at ambient temperatures (Berman *et al.*, 1992). However, to our knowledge no systematic radiation-damage MX studies have been described so far which show specific changes within the native DNA and/or RNA molecule. This might be related to the fact that DNA itself is a very stable molecule (Halliwell & Gutteridge, 1999). Indeed, our own studies (Ravelli *et al.*, unpublished results) did not show any specific damage on cryocooled native RNA or DNA crystals when difference electron-density maps were calculated in similar ways to those that revealed specific damage for proteins (Ravelli & McSweeney, 2000; Weik *et al.*, 2000). However, *R*-factors such as the pairwise decay *R*-factor (Diederichs, 2006) do show signs of radiation damage; this damage seems to be global rather than specific. In contrast, highly specific damage was observed for brominated nucleotides (Ennifar *et al.*, 2002; Ravelli *et al.*, 2003; Schiltz *et al.*, 2004), where debromination was shown to occur rapidly, even at 100 K.

The seeming contradiction between the general observation of single- and double-strand breakages in DNA in solution at low doses (a few Gy; Coggle, 1983) *versus* the absence of MX publications on specific radiation damage in native DNA/RNA crystals either at room temperature (>kGy) or on cryocooled crystals (>MGy) calls for a more careful evaluation of the MX technique.

Crystallography gives a space- and time-averaged structure of the macromolecule. Occupancies well below 10% (Genick *et al.*, 1998; Kort *et al.*, 2004) are unlikely to be observed, even though they could well be present within the crystal. Verification of the existence of certain (low-occupancy) states could benefit from the use of additional techniques such as X-ray fluorescence, UV/Vis fluorescence, fluorescence lifetime, UV/Vis absorbance microspectroscopy (Pearson *et al.*, 2004) and Raman spectroscopy.

Raman microspectroscopy is a powerful technique capable of providing detailed information about the chemical nature of individual bonds. Owing to the intricate molecular make-up of proteins and nucleic acids, the resulting Raman spectra are correspondingly complex. However, when the technique is applied to macromolecular crystals, it offers distinct advantages compared with solutions (reviewed by Carey, 2006): typical macromolecular crystals have a 10- to 100-fold higher concentration and relatively low solvent content, which together improve the Raman signal-to-noise ratio substantially. In addition, crystal packing forces which reduce high-order movements result in increased resolution of Raman bands.

These factors have led to a recent re-emergence of Raman spectroscopy in structural biology (Carey, 1999). By employing customized Raman probes, it has been possible to identify ligands in single crystals in hanging-drop experiments (Zheng *et al.*, 1999) to characterize ligand binding (Altose *et al.*, 2001) and to trap enzyme-substrate intermediates (Helfand *et al.*, 2003; Padayatti *et al.*, 2005). Raman studies on DNA crystals have identified marker bands that can be used to assign large-scale conformational states directly, moderating the gap between solution and crystalline studies (Benevides *et al.*, 1986, 1993). Indeed, with the advent of CCD detectors

sensitive in the red-light region, longer-wavelength lasers can be used thus avoiding luminescence at lower excitation wavelengths. Precision holographic notch filters have become available with increased efficiency to remove elastically scattered photons: it is now possible to measure detailed backbone orientations, ring torsions and individual bond chemistry in nucleic acids. Laser-induced photochemistry is minimized as a direct consequence of Raman sensitivity permitting measurements under non-resonance conditions (Carey, 1999).

In this report we have used a Raman instrument that was recently installed at the Cryobench of the ESRF (http://www.esrf.fr/UsersAndScience/Experiments/MX/Cryobench/Instruments/raman/: Carpentier, Royant & Bourgeois, unpublished results) both offline and online. We name this technique macromolecular crystallography combined with online Raman scattering (MXRS) and demonstrate that it has a sensitivity capable of detecting radiation-damage-induced changes in DNA crystals with exquisite resolution and reproducibility. We unambiguously identify the breakage of a single carbon–bromine covalent bond within DNA crystals by both MX and Raman techniques. In this initial study we aim to determine the quality and reproducibility of the Raman technique and provide a direct comparison and validation using MX. Our report paves the way for future studies on difference Raman spectra and eventually on the assignment of specific X-ray-induced chemical changes within DNA crystals.

2. Materials and methods

2.1. DNA preparation and crystallization

All DNA oligonucleotides were synthesized and HPLC purified by ATDBio, Southampton, UK. The lyophilized DNA was re-suspended in 10 mM HEPES, pH 6.6, diluted to 1 mM and the self-complementary strands were annealed by heating to 343 K followed by slow cooling. DNA was stored at 253 K until required. A sequence consisting of 5′ CGCTGGAAA-CGCTGGAAATTTCCAGC 3′ was chosen, being one of the longest *B*-DNA sequences deposited in the Protein Data Bank (PDB) (1SGS; Huang *et al.*, 2005). Crystallization screens were carried out at the High Throughput Crystallization Laboratory of the EMBL Grenoble Outstation, yielding several hits. Following the initial structural solution of the 17mer we found that the 5′ cytosine was relatively disordered, and indeed crystallization using a truncated 16mer yielded better diffracting crystals. Reproducible high-quality crystals were grown using the hanging-drop vapour diffusion method with 1 μl 1 mM DNA plus 1 μl reservoir solution against 1 ml of 34% PEG 200, 600 mM CaCl$_2$ and 10 mM HEPES pH 8.6. Crystals were visible after several hours and grew to approximate dimensions of 0.5 mm × 0.2 mm × 0.2 mm within one week. Additives such as spermine, present in the 1SGS crystallization buffer, and spermidine did not improve crystal quality and were thus omitted. Subsequent oligonucleotides were synthesized incorporating the modified phosphoramidite 8-bromo-2′-deoxyguanosine at either one position (position 4) or two positions (5 and 15). The double-brominated oligo-

nucleotide was subjected to matrix-assisted laser desorption ionization (MALDI) mass spectrometry which showed that approximately 90% of the starting DNA had two intact C—Br bonds [molecular weight = 5044 (5) Da] while the remaining 10% contained a single bromine [molecular weight = 4965 (5) Da]. These values are in agreement with the expected values of 5039 Da and 4960 Da. No fully debrominated species were detected. The brominated DNA was crystallized under identical conditions. All DNA crystals could be produced reproducibly, allowing us to collect comparable MX and Raman data for different batches of DNA.

2.2. X-ray crystallography

Both the MX and the online Raman data were collected at the European Synchrotron Radiation Facility (ESRF), Grenoble, France. The MX data that were used for the refinement of the DNA model as a function of dose were collected on the MAD beamline ID14-EH4 (see below). The online Raman data were collected on beamline ID14-EH2, as described in §2.4.

Twenty successive complete data sets were collected on ID14-EH4 at a wavelength of 0.976 Å (12.7 keV) within a total time span of 1.5 h using a Q315r 3×3 mosaic CCD from ADSC. The data were collected over identical absolute rotation ranges from the same volume of the same dibrominated 16mer DNA crystal that was flash-cooled into a 100 K Oxford Cryosystems 700 series nitrogen gas stream. The PEG 200 solution had the advantage over the original 1SGS condition of PEG 3350 that it also served as an effective cryoprotectant. Great care was taken to use the maximum amount of beam attenuation to avoid overloads at low resolution but still yielding high-resolution data with a 1 s frame^{-1} exposure time. The beam was attenuated to about 8% of its original intensity and all data sets were processed to 1.6 Å resolution. The crystal belongs to space group $H32$ with averaged cell dimensions of $a = 38.601$ and $c = 159.52$ Å (rhombohedral setting $R32$, $a = b = c = 57.655$ Å, $\alpha = \beta = \gamma = 39.116°$). All data sets were processed using XDS (Kabsch, 1988) and scaled using $XSCALE$. The radiation-damage-induced phasing (RIP; Ravelli et al., 2003) option in the program $SHELXC$ was used to combine pairs of data sets in order to produce ΔFs, while allowing the later data sets to be downscaled by a factor K (Nanao et al., 2005). The program $SHELXD$ (Schneider & Sheldrick, 2002) was used to determine the most susceptible part of the specific radiation damage substructure. All $SHELXD$ processes were run for 50 cycles in Patterson seeding mode. Optimal scale factors K were identified on the basis of the correlation coefficient CC(best) between the observed and calculated radiation-damage substructure normalized structure factors. The program $SHARP$ (La Fortelle & Bricogne, 1997) was used to refine the positions, B-factors and occupancies of the radiation-damage-susceptible substructure against the difference intensities between each data set. The occupancies of the most susceptible atoms could be modelled with a single exponential function $q(d) =$ $c \exp(-d/D)$, where d is the dose, c is a constant and D is the decay constant (Ennifar et al., 2002; Schiltz et al., 2004).

For each oscillation scan, parameters such as shutter status, φ angle and beam intensity were collected for multiple time points using a multi-purpose unit for synchronization, sequencing and triggering (MUSST) card that has been custom-built at the ESRF (Nurizzo et al., 2006). This allowed for each frame an accurate integration of the 100 μm $\times$ 100 μm photon flux that was matching the best diffracting part of the 350 μm $\times$ 100 μm $\times$ 100 μm crystal. The beam intensity counter, positioned between the fast shutter and the crystal, was calibrated against a windowless PIN reference diode from Hamamatsu. The total integrated dose per data set, as calculated using the program $RADDOSE$ (Murray et al., 2004), was about 2.5×10^5 Gy, based on an attenuated flux of 1×10^{11} 12.7 keV photons s^{-1}.

2.3. Raman spectroscopy

A Raman spectrometer (Renishaw, UK) has been adapted for use on a goniometer, either at the Cryobench laboratory or on a macromolecular crystallography beamline at the ESRF, France (http://www.esrf.fr/UsersAndScience/Experiments/MX/Cryobench/Instruments/raman/). It is equipped with a 1200 lines mm^{-1} grating, a dielectric filter, a near-infrared 785 nm laser producing 50 mW at the sample position, and a compact back-scattering probe with a focal spot of 50 μm.

For offline measurements at the Cryobench laboratory, crystals were pre-aligned using the Raman signal from a repeating 1 s laser pulse with a narrow spectral range centred on the major band at 796 cm^{-1}. This ensured the optimum orientation to achieve the highest signal-to-noise ratio prior to full spectral acquisition. Non-polarized spectra were collected in the range 200–2000 cm^{-1} using the Synchroscan mode within the manufacturer's $Wire$ Version 2.0 software, allowing acquisition of wide-range artifact-free spectra by synchronizing the grating movement with integration of the CCD readout. Typical exposure times were 300 s at 100% laser power which resulted in a full spectral acquisition time of 22 min. A baseline curve was fitted to each spectrum using a cubic spline algorithm and then subtracted from the spectrum. The offline spectra obtained from different bromine crystals were scaled to the band at 1100 cm^{-1} in order to allow comparison (see §3.2 for details). The lowest background was obtained by collecting Raman spectra on the exposed region of the crystal protruding outside the cryoloop (Fig. 1, inset), which is probably due to the minimal amount of free solvent surrounding the crystal in this orientation. Offline experiments were performed at 100 K, the sample being cooled by a cold N_2 gas stream from an Oxford Cryosystems 600 series Cryostream.

2.4. Online Raman

In order to perform online measurements, the Raman instrument was installed adjacent to the ID14-EH2 beamline and a 20 m-long custom fibre-optic cable was routed into the experimental hutch. The Raman probe was mounted adjacent
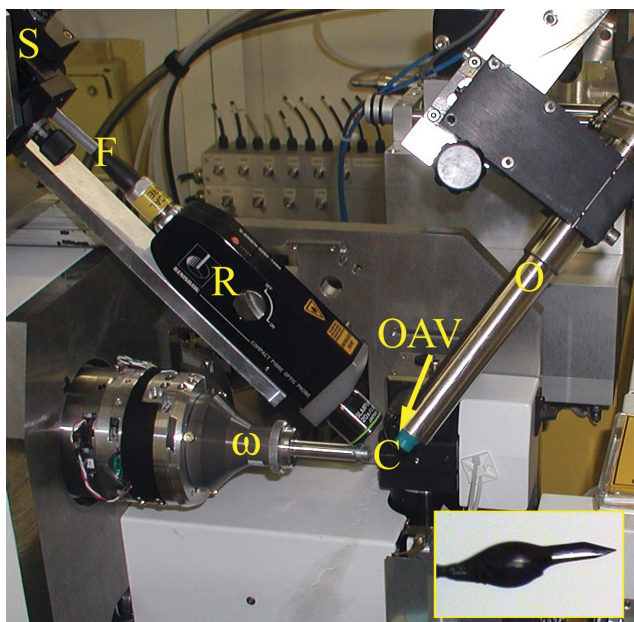
Figure 1
To facilitate online measurements, a Raman back-scattering probe (R) was installed on a custom stage (S) compatible with the minidiffractometer (MD2M) (Maatel, Voreppe, France) on beamline ID14-EH2 at the ESRF, France. A cryocooled crystal (C) was mounted on the spindle axis (ω) and maintained at 100 K by an Oxford Cryosystems 700 series Cryostream (O). The orientation of the X-rays passing through the on-axis visualization unit is shown by an arrow. The X-ray beam and the focal spot of the Raman probe were aligned to be coincident with the crystal. The fibre-optic cable (F) provides the excitation laser input and transfers the Raman scattering to the spectrometer outside the experimental hutch. Crystals were mounted to provide an exposed area free from excess solvent (inset).

to the goniometer head on an MD2M diffractometer (Maatel, Voreppe, France) as shown in Fig. 1. The X-ray beam was localized and the beam size calibrated using a YAG scintillator screen and the on-axis viewing of the microdiffractometer (Perrakis *et al.*, 1999). A 50 µm alignment pinhole mounted at the beam position was used to align the Raman laser focal spot to be coincident with the X-ray beam and then removed. This allowed the Raman laser to probe a region of the crystal that lay within the path of the 400 µm horizontal $\times$ 240 µm vertical X-ray beam. The Raman spectrometer could be controlled in parallel with the MX data collection. Raman spectra were optimized as described in §2.3. All online Raman measurements were collected at identical φ positions, thus minimizing orientation effects during spectral acquisition. Full spectra (200–2000 cm^{-1}) were recorded before and after exposure of the crystals to the X-ray beam. The crystals could also be exposed continuously while collecting region-of-interest (ROI) scans centred at 500 cm^{-1} using single-scan static mode. This resulted in a spectral range of 240–840 cm^{-1} with a total acquisition time of 100 s. An uninterrupted series of ROI spectra were collected with a 2 min repetition time on a fresh dibrominated DNA crystal. The crystals were stationary during X-ray exposure with a dose rate estimated to be 8 $\times$ 10^3 Gy s^{-1} with a flux of 2 $\times$ 10^{11} 13.3 keV photons s^{-1} for a beam size of 100 µm $\times$ 100 µm. Online experiments were

performed at 100 K, the sample being cooled by a cold N$_2$ gas stream from an Oxford Cryosystems 700 series Cryostream.

Baseline subtraction was performed for the ROI series as follows: 18 spectra were scaled together taking the zero-dose spectrum as a reference (program *SCARAM*; Carpentier, unpublished results) allowing subtraction of the general background increase. Good quality fits of spectra could be obtained in the restricted region between 270 cm^{-1} and 380 cm^{-1} using the program *Peakfit* (SeaSolve Software). Integrated intensities of the two Raman bands 293 cm^{-1} (I293) and 335 cm^{-1} (I335) were computed as a function of dose using a Gaussian model with a quadratic polynomial background applied to all spectra.

3. Results and discussion

3.1. Validation of the Raman technique for DNA crystals at 100 K

Fig. 2(*a*) shows Raman spectra of two native DNA crystals mounted in loops at 100 K. The spectra are complex but of good quality. Earlier studies have divided Raman spectra of polynucleotides into three distinct regions based on the technique of vibrational Raman optical activity (ROA; Bell *et al.*, 1997). Although this is an over-simplification of standard non-resonance Raman spectra, it provides a general description of the spectra shown in Fig. 2(*a*). Vibrational bands from the sugar rings are mainly located in the region $\sim$900–
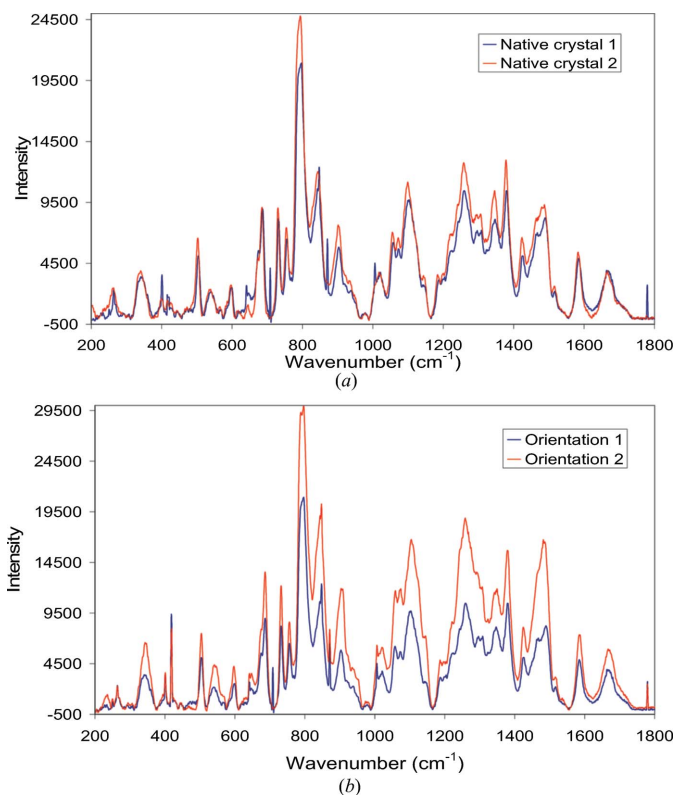
Figure 2
(*a*) Reproducibility between Raman spectra from two different native DNA crystals grown and measured three months apart. (*b*) Orientation effects measured on the same native DNA crystal.

1150 cm^{-1} and correspond to both the sugar ring and phosphate backbone conformations. Bands between ∼1200 cm^{-1} and 1550 cm^{-1} are mainly from sugar-base structures and correspond to normal modes involving mixing of vibrational coordinates from both the base and sugar rings. The third region between ∼1550 cm^{-1} and 1750 cm^{-1} is linked to base-stacking both in terms of the specific base and also stacking arrangement. Many of the bands within these regions overlap significantly and therefore reliable assignment can be problematic. The ROA method has been successfully employed to reduce the inherent complexity of these signatures and has allowed detailed assignments within these regions (Bell et al., 1997). Furthermore, Raman studies on nucleic acids with various base compositions have identified several clearly resolved marker bands which are useful for determining overall conformation (Fabian et al., 1993, and references therein). Two such bands that have been assigned to B-form DNA structures, 685 cm^{-1} and 1421 cm^{-1}, are clearly present in the spectra in Fig. 2 confirming the MX observations (Huang et al., 2005). The strongest band at 796 cm^{-1} is generally assigned in B-form DNA to the complex vibration of the 5′C–O–P–O–C3′ network with possible overlap with marker bands from thymine and cytosine at 790 cm^{-1} and 780 cm^{-1} (Deng et al., 1999).

It has previously been shown that in nucleic acid crystals the Raman contribution from the solvent is very low due to the high concentration of DNA in the crystal (Benevides et al., 1984). In order to confirm this for our conditions, a control spectrum was collected from solvent solution and major bands were observed at 354 cm^{-1}, 845 cm^{-1}, 1284 cm^{-1} and 1478 cm^{-1} with several additional low-intensity bands. Although most of these bands overlap with DNA bands, there is a useful solvent marker at 315 cm^{-1} which is not present in the DNA spectrum. This band was employed to scale the solvent spectrum to the DNA spectrum, revealing that the maximum solvent contribution at the most intense solvent band is less than 5% of the total Raman signal collected from the DNA crystal.

Reproducibility between individual crystals is high, as demonstrated in Fig. 2(a) which shows Raman spectra from two crystals that were grown three months apart. The spectra are in general agreement although some grouped bands have small intensity variations which most likely reflect differences in orientation effects and background subtraction. For example, it is notable that in the region 1200–1400 cm^{-1} the intensities of all bands are increased relative to each other by approximately 20% but in general all bands are present in the two spectra. Fig. 2(b) shows the differences directly attributable to a re-orientation of a crystal relative to the Raman laser position. Again no new bands appear or disappear between the two spectra; however, there are clear differences in scaling with relative shifts in the same region, 1200–1400 cm^{-1}, between 30 and 50%. The difference in scaling between some individual bands relative to the orientation of the probe and the crystal reflects the complex contributions of both symmetric and non-symmetric vibrations to the full Raman spectrum (Kudryavtsev et al., 1998; Carey, 1982).

3.2. Offline Raman studies of brominated oligonucleotides

The Raman spectra of crystals in which the starting DNA had been chemically modified with either one or two 8-bromo-deoxyguanosine bases were compared with those collected on native crystals (Fig. 3). In order to perform a direct comparison of three different crystals it was necessary to scale these spectra to a reference band. The band at 1100 cm^{-1} is very characteristic of DNA and RNA Raman spectra and has been
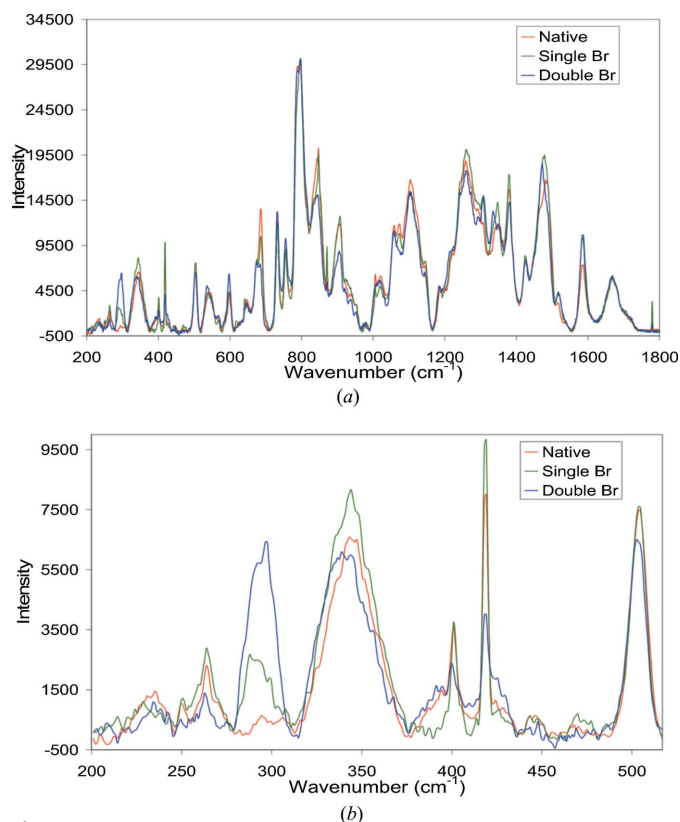
Figure 3
(a) Raman spectrum of a native DNA crystal compared with spectra from brominated and dibrominated crystals. Spectra were scaled to the PO$_2^-$ band at 1100 cm^{-1}. (b) Zoomed spectra of the low vibrational region including the bromine-specific band at 293 cm^{-1}.
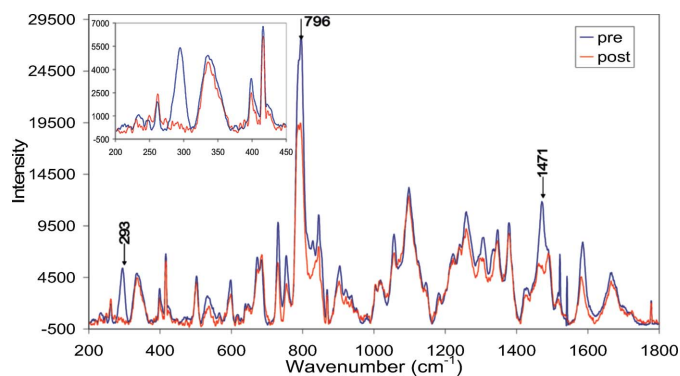
Figure 4
Online Raman spectra on the same crystal, at the same orientation, before and after X-ray exposure. Major band intensity changes are marked with arrows (see text for details). The inset shows the zoomed region, 200–450 cm^{-1}, and details the clear reduction of the 293 cm^{-1} band.

previously assigned to the PO_2^- symmetrical stretch motion (Tsuboi *et al.*, 1971). The frequency and intensity are insensitive to backbone geometry; this band therefore provides a useful internal standard (Tsuboi *et al.*, 1971) so it was used for scaling in this case. Despite the potential sensitivity of this band to crystal orientation as a consequence of its symmetry, it can be observed in Fig. 3 that the majority of bands are successfully superimposed using this single scale factor. The strongest band at 796 cm^{-1} appears to be largely unaffected by bromination of the guanines.

Fig. 3 shows the clearly resolved band centred at 293 cm^{-1} which is visible in the two brominated DNA crystals but only shows a baseline signal for the native crystal. Notably, the single bromine crystal has a peak area ratio of 0.5 compared with the peak from the crystal containing two brominated guanines. If one assumes equal contribution of each of the covalently-bound bromine atoms in each DNA crystal, then the peak area at 293 cm^{-1} can be used to quantify the number of intact C—Br bonds. The relative intensity of the 293 cm^{-1} band does not vary significantly with crystal orientation relative to reference bands since the bending mode of the C—Br bond is non-symmetric (Carey, 1982; Schrumpf & Dunker, 1986).

Further differences are apparent, including a possible shift from the native band at 1487 cm^{-1} to 1474 cm^{-1} in the single-bromine and to 1471 cm^{-1} in the double-bromine crystal. A similar shift has been reported in previous studies comparing Raman spectra of guanosine and 8-bromo-guanosine in solution [band shift from 1490 cm^{-1} to 1473 cm^{-1} (Chinsky *et al.*, 1978)]. This shift has been previously assigned to a combination of stretching and bending ring vibrations particularly centred around the N_7 and C_8 position of guanine (Mansey & Peticolas, 1976). A significant decrease in the 685 cm^{-1} band is seen in the brominated crystals; this band is normally assigned to guanine (Fabian *et al.*, 1993). It is sensitive to the orientation of the guanine residue relative to the ribose ring structure and may be a useful reporter for the presence of a bromine atom at the C_8 position (Nishimura *et al.*, 1983, 1984).

Many of the C—Br bands are situated in crowded regions of the spectrum and are therefore sensitive to scaling and background subtraction differences. In addition, these band intensities are not always proportional to the number of C—Br bonds in each duplex. Since the spectrum of the native DNA crystal has few low-frequency bands in the region 278–314 cm^{-1}, the band at 293 cm^{-1} represents an excellent Raman marker for the C—Br bond (Fig. 3b). The typical tabulated values of the higher-intensity C—Br vibrational modes visible by Raman spectroscopy are between 500 cm^{-1} and 700 cm^{-1}; however, detailed studies on small molecules such as halogen-substituted cyclopropanes have allowed unambiguous assignments of several C—Br bending modes in the 106–386 cm^{-1} region (Schrumpf & Dunker, 1986).

Tests were performed on DNA crystals containing other commercially available brominated bases including 8-bromo-2′-deoxyadenosine and 5-bromo-2′-deoxycytidine. Significantly, no band was seen at 293 cm^{-1} with brominated cytidine DNA crystals; however, a similar signature band at 299 cm^{-1}

was seen with the 8-deoxy-2′-adenosine modification (data not shown). The technique reported here is therefore able to discriminate between a bromine bond on the C8 position of the purine ring and on the C5 position of the pyrimidine ring.

3.3. Online Raman studies

The online Raman set-up was used to directly follow X-ray-induced DNA damage within the cryocooled crystal. Fig. 4 shows the full Raman spectra collected before and after exposing a double-brominated DNA crystal to 40 min of unattenuated X-ray beam on ID14-2 (estimated dose 2.4 × 10^7 Gy). Inspection of the uncorrected data without background subtraction and scaling (not shown) demonstrates that the background increases almost threefold during the 40 min exposure to X-rays. The spectra in Fig. 4 have therefore been baseline-corrected. As the two spectra were collected on the same spot on the same crystal they can be related without additional scaling. This allows direct comparison of the X-ray-induced chemical changes without the perturbations, such as orientation effects, present in the offline experiments. The C—Br marker at 293 cm^{-1} shows an extremely clear X-ray-induced debromination of the DNA. The other peaks in the 200–500 cm^{-1} region remain more or less uneffected.

There is a large decrease at 796 cm^{-1} but, since this band corresponds to overlapping vibrations from thymine, cytosine and the backbone, it is difficult to assign this directly to a specific site. The bromine specific band around 1471 cm^{-1} (see also §3.2) undergoes a dramatic change upon X-ray irradiation. Given that it represents vibrations in the C8 guanine, it is likely to be directly correlated with the debromination.

3.4. Debromination followed by online Raman

A series of ROI Raman spectra were collected within a reduced spectral acquisition window between 240 cm^{-1} and 840 cm^{-1} whilst the stationary double-brominated crystal was exposed to the X-ray beam. The 19 Raman spectra collected over 36 min X-ray exposure showed a significant overall average intensity increase up to 50%. Following a dramatic increase of 17% in the first spectrum collected after initial X-ray exposure, there was an almost linear X-ray-induced increase in the Raman background signal. It is possible that this increase is related to optical changes in the vitrified solvent, and further studies, such as online absorption and fluorescence, may provide light on this. The scaling program *SCARAM* (Carpentier, unpublished results) provides a convenient method of subtracting this background from the spectra and, since the crystal remains in the same orientation, no further scaling is necessary.

X-ray-induced debromination could be monitored in real time. Fig. 5(a) shows a series of ROI spectra as a function of dose with the decay of the 293 cm^{-1} band clearly visible. The integrated intensity of the 293 cm^{-1} band (I293) is directly proportional to the number of C—Br bonds and declines with the X-ray dose. In contrast, the adjacent 335 cm^{-1} band (its integrated intensity is named I335) is relatively stable and assumed to be independent of damage. The ratio I293/I335 is

Table 1
Selected data-collection statistics for a series of 20 data sets collected on a dibrominated DNA crystal.

The space group is $H32$ with average cell dimensions of $a = 38.601$ (0.023) and $c = 159.52$ (0.098) Å calculated using XDS (rhombohedral setting $R32$, $a = b = c = 57.655$ Å, $\alpha = \beta = \gamma = 39.116°$). The total dose delivered during all 20 data sets was 4.9×10^6 Gy.

	Set 1	Set 5	Set 15	Set 20
Unit-cell parameters (Å)	$a = 38.58$, $c = 159.33$	$a = 38.59$, $c = 159.38$	$a = 38.61$, $c = 159.62$	$a = 38.62$, $c = 159.71$
No. of reflections	19132 (3022)	19169 (3066)	19130 (3048)	19148 (3066)
No. of unique reflections	6112 (937)	6124 (950)	6114 (947)	6119 (953)
Completeness (%)	96.1 (94.5)	95.9 (90.3)	96.1 (95.8)	96.0 (95.9)
$\langle I/\sigma(I) \rangle$	13.9 (2.9)	12.4 (2.4)	13.8 (2.4)	13.0 (2.1)
R-factor (%)†	5.1 (42.0)	5.7 (51.0)	5.0 (52.4)	5.4 (60.9)
Redundancy	3.1	3.1	3.1	3.1
Dose/data set (Gy)	2.5×10^5	2.3×10^5	2.9×10^5	2.8×10^5

† R-factor is $\Sigma|I(\bar{h}, i) - I(\bar{h})|/\Sigma I(\bar{h})$, where $I(\bar{h})$ is the intensity of the reflection with index $\bar{h}$, and $I(\bar{h}, i)$ is the intensity of the symmetry-related (i) reflection with index $\bar{h}$. Data are given for resolution 40.0–1.60 Å and numbers in brackets refer to the highest shell, 1.70–1.60 Å.

used as a direct measure of the occupancies of the C—Br bonds and has been plotted as a function of dose d (Fig. 5b). The resulting curve can be fitted with a single exponential, $q(d) = 0.97 \exp(-1.4 \times 10^{-7} \times d)$ with an R^2 value of 0.977. This corresponds to a decay constant (D) of 7.1 MGy. This decay constant is only slightly smaller than those reported (between 7.4 and 9.2 MGy) by Ennifar *et al.* (2002).

3.5. Dose-dependent occupancy refinement

The dose-dependent debromination measured by MXRS can be directly validated using MX. Indeed, specific damage to the C—Br bond can be used, as demonstrated before (Ravelli *et al.*, 2003; Schiltz *et al.*, 2004), for phasing of the MX data through the RIP method. Table 1 shows the statistics of some of the 20 data sets collected on ID14-EH4, whereas Table 2 shows statistics obtained using *SHELXC* and *SHELXD* (Schneider & Sheldrick, 2002; Nanao *et al.*, 2005). Within four data sets, corresponding to a dose of 1 MGy, large intensity changes can be observed, *e.g.* the average intensity difference between the first and the fourth data set is 8.1%. These differences are readily interpreted by the program *SHELXD*, which finds both Br sites with excellent statistics for the correlation coefficients (CC$_{\text{best}}$ and CC$_{\text{weak}}$) between the observed and calculated radiation-damage substructure normalized structure factor.

Ramagopal *et al.* (2005) showed how the radiation-induced decomposition of mercury adducts resulted in complete loss of mercury signal at higher doses. However, our Raman studies show that the C—Br bond, despite being the most susceptible bond, is reduced but not obliterated at higher X-ray doses (Fig. 5a). For example, at 3 MGy the 293 cm^{-1} peak has been reduced to half of its original integrated intensity, whereas this is still about a quarter at 12 MGy.

In order to further investigate the decay of the electron density for the bromine atoms *versus* dose, the program *SHARP* was used which allowed accurate refinement of the occupancies of these atoms against the intensity differences between the data sets. The results are shown in Fig. 5(c). The different exponential decay of both bromine atoms proved to be beneficial for phasing. The radiation-damage-susceptible substructure was, incidentally, almost perfectly centrosym-
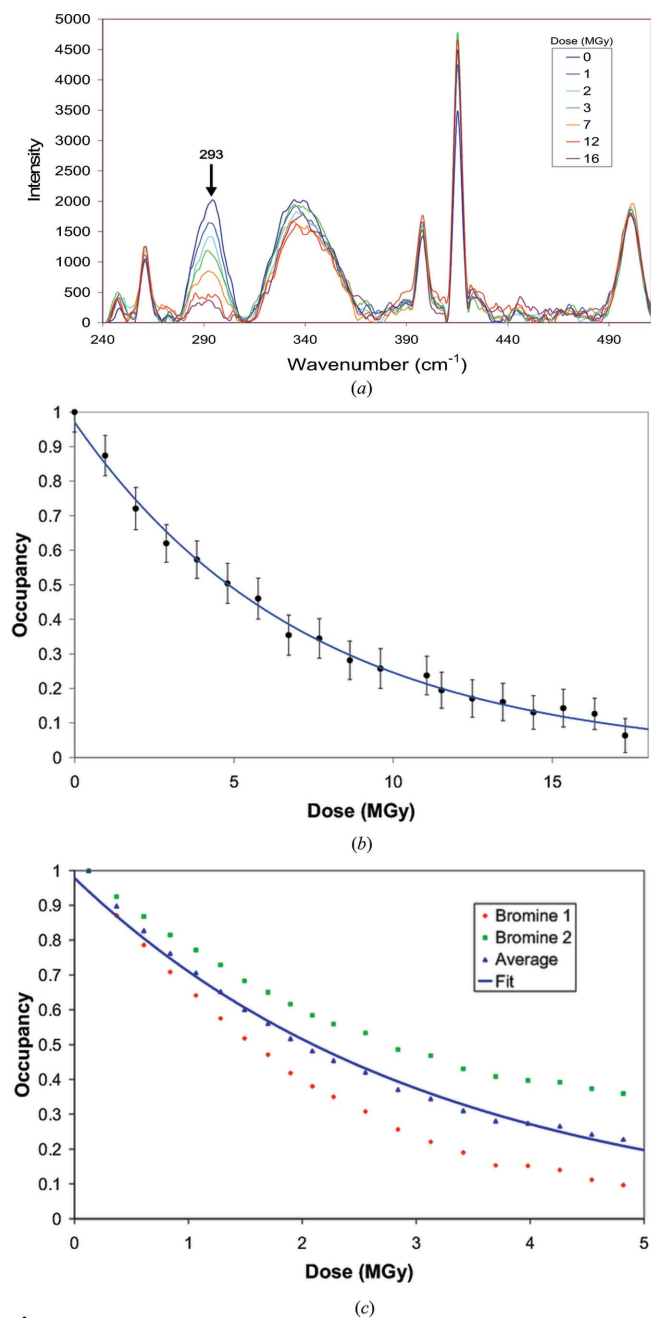
Table 2
SHELXD statistics for RIP phasing.

The first data set was always used as the reference data set. The scale factor K is used to downscale the later data sets, as described by Nanao *et al.* (2005). R_{int} is $\Sigma|I - \langle I \rangle|/\Sigma I$ when comparing the intensities from the first and the later data sets with their averaged values. The correct substructure was found for each set.

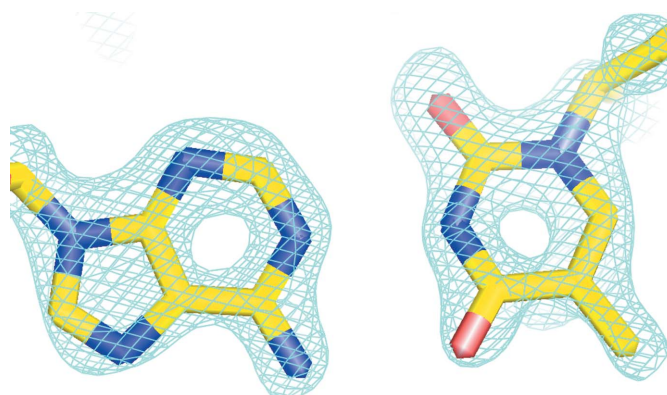| Set	CC(best)	CC(weak)	K	R_{int}
2	27.4	19.4	0.986	0.049
3	46.7	30.0	0.989	0.062
4	54.1	36.1	0.983	0.081
5	60.1	40.8	0.983	0.096
6	63.7	43.7	0.977	0.113
7	63.8	42.8	0.977	0.126
8	64.8	46.0	0.967	0.140
9	64.6	46.3	0.971	0.154
10	64.4	44.5	0.967	0.165
11	65.2	45.6	0.977	0.174
12	65.8	48.4	0.957	0.184
13	66.0	48.6	0.957	0.196
14	65.5	48.0	0.947	0.208
15	63.7	46.4	0.961	0.221
16	64.3	48.4	0.941	0.235
17	63.8	48.0	0.949	0.242
18	62.8	46.0	0.961	0.251
19	63.2	47.9	0.935	0.259
20	62.2	45.4	0.943	0.266

metric within our crystal form. This prevents powerful density modification programs such as *SHELXE* (Sheldrick, 2002) overcoming the phase ambiguity in RIP, resulting in maps that showed the original structure superimposed on its mirror image. In contrast, the program *SHARP* (La Fortelle & Bricogne, 1997) provided reasonable experimental maps (Fig. 6) by exploiting the differences in exponential decay as well as a knowledge of the partial structure consisting of two bromine atoms, which make a significant contribution to the native structure factors. The occupancies of the bromine atoms, as refined using *SHARP*, show two different decay curves (Fig. 5c). The average bromine occupancy *versus* dose function could be fitted with a single exponential, $q(d) = 0.98 \exp(-3.2 \times 10^{-7} \times d)$ with an R^2 value of 0.991. This corresponds to an average decay constant of 3.1 MGy. Decay constants of 2.0 MGy and 4.5 MGy were obtained for the two individual bromine atoms with fits to the exponentials $q(d) =$

Figure 6

Region of experimental RIP electron density contoured at 1.2σ showing an adenine (position 7)–thymine (position 10′) base pair. The maps are shown after phasing and solvent flattening through *SHARP* (La Fortelle & Bricogne, 1997).

et al. (2002), and the individual exponential decay parameters of $6.7\ \mathrm{MGy^{-1}}$ and $7.1\ \mathrm{MGy^{-1}}$ compare favourably with those reported here.

4. Conclusions

X-ray-induced radiation damage in macromolecular cryo-cooled crystals induces a multitude of chemical and physical changes within the crystal and its surrounding liquid. Some changes might be visible in electron-density difference maps calculated between successive data sets, thus highlighting strongly preferred pathways that cause similar changes in most unit cells of the crystal. Other changes could be different within each unit cell, thus contributing to the gradual degradation of the crystalline diffractive power. These changes might include alterations that radiation chemists would know to be 'specific', whereas they would be labelled 'general damage' by the macromolecular crystallographer.

We are not aware of any MX studies that describe X-ray-induced 'specific damage' in native polynucleotide crystals. However, a detailed structural observation of the consequences of radiation-induced damage of DNA could be of great relevance. It is somewhat puzzling that cryocooled protein crystals show clear signs of 'specific damage' in contrast to those of native polynucleotides. We therefore investigated the use of complementary techniques to monitor changes in cryocooled DNA crystals occurring during MX data collection.

We explored the use of Raman spectroscopy online on a synchrotron MX beamline to monitor changes within a crystal upon X-ray exposure. MXRS measurements offer the possibility of looking at very fine details and changes in the chemistry of crystalline macromolecules. Indeed, because the Raman effect is enhanced by the low solvent contribution, high target concentration and decreased line-width due to low temperature, the online technique offers many advantages over solution measurements as well as over other MX complementary methods such as fluorescence and UV/Vis spectroscopy. It is shown that reproducible high-quality

Figure 5

(*a*) Real-time Raman online ROI monitoring of a double-brominated DNA crystal during continuous X-ray exposure on beamline ID14-EH2. Debromination can be followed from the decay of the $293\ \mathrm{cm^{-1}}$ band as a function of dose. (*b*) Bromine occupancy calculated from the ratio of integrated intensities of the Raman bands $293\ \mathrm{cm^{-1}}$ and $335\ \mathrm{cm^{-1}}$ (I293/I335) as a function of X-ray dose. The data can be fitted to the single exponential $q(d) = 0.97\exp(-1.4 \times 10^{-7} \times d)$ with an R^2 value of 0.991 and corresponds to a decay constant of 7.1 MGy. (*c*) Bromine occupancy refined using *SHARP* against 20 MX data sets collected on ID14-EH4 as a function of dose. The averaged data can be fitted to the single exponential $q(d) = 0.98\exp(-3.2 \times 10^{-7} \times d)$ with an R^2 value of 0.991 and corresponds to a decay constant of 3.1 MGy.

$1.07\exp(-5.0 \times 10^{-7} \times d)$ (R^2 value of 0.998) and $q(d) = 0.97\exp(-2.2 \times 10^{-7} \times d)$ (R^2 value of 0.984), respectively. Schiltz *et al.* (2004) also reported different susceptibility of two bromine atoms within an RNA crystal as measured by Ennifar

Raman data can be obtained down to 200 cm^{-1}. We have used MXRS to follow the breakage and measure the dose-dependent decay of the highly X-ray susceptible C—Br bond. The decay functions of the two bromine atoms have been quantified using MX data and have been correlated with the decay of peaks that could be unambiguously assigned within the Raman spectra.

Several factors must be taken into account when comparing these two independent methods for determining debromination. We used two different beamlines, ID14-EH2 and ID14-EH4 for MXRS and MX, respectively, thus differences in flux calibration, beam shape and crystal parameters will make it harder to obtain a good quantitative comparison. However, the agreement of the calculated decay constants between MXRS (Fig. 2b) and MX (Fig. 2c), and indeed compared with previously published studies, is remarkable and clearly validates MXRS as a highly sensitive and reliable method to measure X-ray-induced debromination in DNA crystals.

The unambiguous assignment of one peak in the Raman spectra of DNA crystals and the correlation of its decay as followed both by Raman and MX makes us optimistic that the combined use of Raman and MX could provide an unique way to study the multitude of events that occurs when radiation damages crucial biomolecules.

References

Altose, M. D., Zheng, Y., Dong, J., Palfey, B. A. & Carey, P. R. (2001). *Proc. Natl. Acad. Sci. USA*, **98**, 3006–3011.

Bell, A. F., Hecht, L. & Barron, L. D. (1997). *J. Am. Chem. Soc.* **119**, 6006–6013.

Benevides, J. M., Wang, A. H., Rich, A., Kyogoku, Y., van der Marel, G. A., van Boom, J. H. & Thomas, G. J. Jr (1986). *Biochemistry*, **25**, 41–50.

Benevides, J. M., Wang, A. H. & Thomas, G. J. Jr (1993). *Nucl. Acids Res.* **21**, 1433–1438.

Benevides, J. M., Wang, A. H., van der Marel, G. A., van Boom, J. H., Rich, A. & Thomas, G. J. Jr (1984). *Nucl. Acids Res.* **12**, 5913–5925.

Berman, H. M., Olson, W. K., Beveridge, D. L., Westbrook, J., Gelbin, A., Demeny, T., Hsieh, S. H., Srinivasan, A. R. & Schneider, B. (1992). *Biophys. J.* **63**, 751–759.

Boudaiffa, B., Cloutier, P., Hunting, D., Huels, M. A. & Sanche, L. (2000). *Science*, **287**, 1658–1660.

Burmeister, W. P. (2000). *Acta Cryst.* D**56**, 328–341.

Carey, P. R. (1982). *Biochemical Applications of Raman and Resonance Raman Spectroscopies*. New York: Academic Press.

Carey, P. R. (1999). *J. Biol. Chem.* **274**, 26625–26628.

Carey, P. R. (2006). *Annu. Rev. Phys. Chem.* **57**, 527–554.

Chinsky, L., Turpin, P. Y., Duquesne, M. & Brahms, J. (1978). *Biopolymers*, **17**, 1347–1359.

Coggle, J. E. (1983). *Biological Effects of Radiation*, 2nd ed. New York: Taylor and Francis.

Deng, H., Bloomfield, V. A., Benevides, J. M. & Thomas, G. J. Jr (1999). *Biopolymers*, **50**, 656–666.

Diederichs, K. (2006). *Acta Cryst.* D**62**, 96–101.

Ennifar, E., Carpentier, P., Ferrer, J.-L., Walter, P. & Dumas, P. (2002). *Acta Cryst.* D**58**, 1262–1268.

Fabian, H., Hölzer, W., Heinemann, U., Sklenar, H. & Welfle, H. (1993). *Nucl. Acids Res.* **21**, 569–576.

Favaudon, V., Tourbez, H., Houee-Levin, C. & Lhoste, J. M. (1990). *Biochemistry*, **29**, 10978–10989.

Genick, U. K., Soltis, S. M., Kuhn, P., Canestrelli, I. L. & Getzoff, E. D. (1998). *Nature (London)*, **392**, 206–209.

Halliwell, B. & Gutteridge, J. (1999). *Free Radicals in Biology and Medicine*, 3rd ed. Oxford University Press.

Helfand, M. S., Totir, M. A., Carey, M. P., Hujer, A. M., Bonomo, R. A. & Carey, P. R. (2003). *Biochemistry*, **42**, 13386–13392.

Helliwell, J. R. (1988). *J. Cryst. Growth*, **90**, 259–272.

Huang, D.-B., Phelps, C. B., Fusco, A. J. & Ghosh, G. (2005). *J. Mol. Biol.* **346**, 147–160.

Kabsch, W. (1988). *J. Appl. Cryst.* **21**, 916–924.

Kort, R., Hellingwerf, K. J. & Ravelli, R. B. (2004). *J. Biol. Chem.* **279**, 26417–26424.

Kudryavtsev, A. B., Mirov, S. B., DeLucas, L. J., Nicolete, C., van der Woerd, M., Bray, T. L. & Basiev, T. T. (1998). *Acta Cryst.* D**54**, 1216–1229.

La Fortelle, E. de & Bricogne, G. (1997). *SHARP: A Maximum-Likelihood Heavy-Atom Parameter Refinement Program for the MIR and MAD Methods*. Orlando, FL: Academic Press.

Mansey, S. & Peticolas, W. L. (1976). *Biochemistry*, **15**, 2650–2655.

Michael, B. D. & O'Neill, P. (2000). *Science*, **287**, 1603–1604.

Murray, J. W., Garman, E. F. & Ravelli, R. B. G. (2004). *J. Appl. Cryst.* **37**, 513–522.

Nanao, M. H., Sheldrick, G. M. & Ravelli, R. B. G. (2005). *Acta Cryst.* D**61**, 1227–1237.

Nishimura, Y., Tsuboi, M., Nakano, T., Higuchi, S., Sato, T., Shida, T., Uesugi, S., Ohtsuka, E. & Ikehara, M. (1983). *Nucl. Acids Res.* **11**, 1579–1588.

Nishimura, Y., Tsuboi, M. & Sato, T. (1984). *Nucl. Acids Res.* **12**, 6901–6908.

Nurizzo, D., Mairs, T., Guijarro, M., Rey, V., Meyer, J., Fajardo, P., Chavanne, J., Biasci, J.-C., McSweeney, S. & Mitchell, E. (2006). *J. Synchrotron Rad.* **13**, 227–238.

Padayatti, P. S., Helfand, M. S., Totir, M. A., Carey, M. P., Carey, P. R., Bonomo, R. A. & van den Akker, F. (2005). *J. Biol. Chem.* **280**, 34900–34907.

Pearson, A. R., Mozzarelli, A. & Rossi, G. L. (2004). *Curr. Opin. Struct. Biol.* **14**, 656–662.

Perrakis, A., Cipriani, F., Castagna, J. C., Claustre, L., Burghammer, M., Riekel, C. & Cusack, S. (1999). *Acta Cryst.* D**55**, 1765–1770.

Ramagopal, U. A., Dauter, Z., Thirumuruhan, R., Fedorov, E. & Almo, S. C. (2005). *Acta Cryst.* D**61**, 1289–1298.

Ramakrishna, D. N., Symons, M. C. R. & Stephenson, J. M. (1983). *J. Chem. Soc. Perkin Trans. II*, pp. 727–730.

Ravelli, R. B. G., Leiros, H.-K. S., Pan, B., Caffrey, M. & McSweeney, S. (2003). *Structure*, **11**, 217–224.

Ravelli, R. B. G. & McSweeney, S. M. (2000). *Struct. Fold Des.* **8**, 315–328.

Schiltz, M., Dumas, P., Ennifar, E., Flensburg, C., Paciorek, W., Vonrhein, C. & Bricogne, G. (2004). *Acta Cryst.* D**60**, 1024–1031.

Schneider, T. R. & Sheldrick, G. M. (2002). *Acta Cryst.* D**58**, 1772–1779.

Schrumpf, G. & Dunker, H. (1986). *J. Raman Spectrosc.* **17**, 433–436.

Sheldrick, G. M. (2002). *Z. Kristallogr.* **217**, 644–650.

Symons, M. C. R. (1995). *Radiat. Phys. Chem.* **45**, 837–845.

Tsuboi, M., Takahashi, S., Muraishi, S., Kajiura, T. & Nishimura, S. (1971). *Science*, **174**, 1142–1144.

Weik, M., Ravelli, R. B., Kryger, G., McSweeney, S., Raves, M. L., Harel, M., Gros, P., Silman, I., Kroon, J. & Sussman, J. L. (2000). *Proc. Natl. Acad. Sci. USA*, **97**, 623–628.

Zheng, Y., Dong, J., Palfey, B. A. & Carey, P. R. (1999). *Biochemistry*, **38**, 16727–16732.